

Fifth-degree elastic potential for predictive stress-strain relations and elastic instabilities under large strain and complex loading in Si

Hao Chen,^{1,2,*} Nikolai A. Zarkevich,^{3,†} Valery I. Levitas,^{2,3,4,‡} Duane D. Johnson,^{3,5,§} and Xiancheng Zhang^{1,¶}

¹Key Laboratory of Pressure Systems and Safety, Ministry of Education, School of Mechanical and Power Engineering, East China University of Science and Technology, Shanghai 200237, China

²Department of Aerospace Engineering, Iowa State University, Ames, Iowa 50011, USA

³Ames Laboratory, U.S. Department of Energy, Iowa State University, Ames, Iowa 50011-3020, USA

⁴Department of Mechanical Engineering, Iowa State University, Ames, Iowa 50011, USA

⁵Department of Materials Science & Engineering, Iowa State University, Ames, Iowa 50011, USA

(Dated: February 17, 2020)

Materials under complex loading develop large strains and often transition via an elastic instability, as observed in both simple and complex systems. Here, we represent Si I under large strain in terms of Lagrangian strains by an 5th-order elastic potential found by minimizing error relative to density functional theory (DFT) results. The Cauchy stress – Lagrangian strain curves for arbitrary complex loadings are in excellent correspondence with DFT results, including the elastic instability driving the Si I→II phase transformation (PT) and the shear instabilities. PT conditions for Si I→II under action of cubic axial stresses are linear in Cauchy stresses in agreement with DFT predictions. Such elastic potential permits study of elastic instabilities and orientational dependence leading to different PTs, slip, twinning, or fracture, providing a fundamental basis for continuum simulations of crystal behavior under extreme loading.

Keywords: Elastic potentials of fifth-degree; Elastic instability; Complex loading; Density functional theory; Large strains

INTRODUCTION

Nonlinear, anisotropic elastic properties of single crystals determine material response to extreme loading, e.g., in shock waves, under high static pressure, and in defect-free crystals and nanoregions. Elastic nonlinearity ultimately results in elastic lattice instabilities [1–6]. Such instabilities dictate various phenomena, including phase transitions (PT, i.e., crystal-crystal [7–10], amorphization [11–15], and melting [16, 17]), slip, twinning, and fracture, in particular, theoretical strength in tension, compression, or shear [3–5, 18–20]. In addition, nonlinear elastic properties are necessary for simulations of material behavior under extreme static [21] or dynamic [22, 23] loadings and near interfaces with significant lattice mismatch.

Notably, third-order [24–26] and seldom fourth-order elastic constants [27, 28] are known for different crystals, as determined at small strains (e.g., 0.02–0.03). As such, fourth-order elastic constants “should be treated as an estimation only,” e.g., for Si [28]. Indeed, these elastic constants are not consistent with the observed equation of state of diamond [21]. Extrapolation to large strain is unreliable to describe the lattice instability (e.g., at 0.2 for Si [10] or 0.3–0.4 for B₄C [29, 30]). Thus, to describe correctly elasticity, including any lattice instability, higher-order elastic potentials are required, and must be calibrated for a range of strain including lattice instability. For some loadings, stress-strain curves at finite strains are obtained [4, 5, 10, 18, 19, 29–31], yet this is insufficient for simulation of material behavior or describing lattice instabilities under arbitrary complex or extreme loadings.

Here, an elastic potential of fifth-degree for Si I under large strain was determined in terms of Lagrangian strains (all 6 components) by minimizing error with respect to density functional theory (DFT) results within large strain ranges that

includes instability points. The Cauchy stress – Lagrangian strain curves for multiple complex loadings are in excellent agreement with DFT results, including elastic instability that drives the phase transformation to Si II and shear instabilities. Conditions for Si I→Si II PT under action of cubic axial stresses are found to be linear in Cauchy stresses, as predicted by DFT. Importantly, lower-order potentials cannot yield similar precision in the description of stress-strain curves and elastic instabilities. Obtained elastic potential opens possibility to study all elastic instabilities leading to different PTs, fracture, slip, and twinning, and represents a fundamental basis for continuum simulations of crystal behavior under extreme static and dynamic loading including the above processes and their orientational dependence.

Due to the technological import, the deformation and PT properties of silicon have been studied intensely. The third-order elastic constants were found with DFT [24, 25] and experiments [32, 33]; however, higher-order elastic constants were not reported. The lattice instability under two-parametric loadings was studied in [4, 5, 18, 19]. Lattice instability conditions driving the Si I→II PT under action of the Cauchy stress tensor (6 independent stresses) were obtained in [8, 10], utilizing predictions from the phase field approach [34].

Nonlinear elastic potential. Motion of an elastic body is described by vector function $x_i(X_j, t)$, where t is time and x_i (deformed) and X_j (undeformed reference state) are the Cartesian coordinates of the position vector. The deformation gradient and finite Lagrangian strain are then $F_{ij} = \partial x_i / \partial X_j$ and $\eta_{ij} = \frac{1}{2}(F_{ki}F_{kj} - \delta_{ij})$, respectively, where δ_{ij} is the Kronecker delta (unit tensor) and Einstein summation notation is assumed. Using Voigt notation to simplify presentation, i.e., $\eta_{ii} \rightarrow \eta_i$ (for $i=1,2,3$), and $\eta_{23} \rightarrow \eta_4/2$, $\eta_{31} \rightarrow \eta_5/2$ and $\eta_{12} \rightarrow \eta_6/2$, the specific internal energy per unit undeformed

volume is, as a power-series expansion:

$$u = u_0 + \frac{1}{2}c_{ij}\eta_i\eta_j + \frac{1}{6}c_{ijk}\eta_i\eta_j\eta_k + \frac{1}{24}c_{ijkl}\eta_i\eta_j\eta_k\eta_l + \frac{1}{120}c_{ijklm}\eta_i\eta_j\eta_k\eta_l\eta_m + \dots, \quad (1)$$

where the $c_{...}$ are elastic moduli of second, third, fourth, fifth and higher order. For crystals with cubic symmetry, Eq. (1) is specified in supplemental material [35] in cubic axes, with 3 second-, 6 third-, 11 fourth-, and 18 fifth-order moduli [36], found here using DFT. The second Piola-Kirchhoff (PK2) stress and the true Cauchy stress are defined as

$$S_i = \frac{\partial u}{\partial \eta_i}; \quad \sigma_{ij} = J^{-1}F_{ik}S_{km}F_{jm}; \quad J = \det F_{ik}. \quad (2)$$

We performed DFT simulations supplementing our simulations in [10], especially for shear strains and complex combined compression-shear loadings, and data are in [35]. Parameter identification procedure is carried out and results are presented in the natural cubic coordinate system.

Fitting procedure. Rather than determine certain set of elastic moduli from the distinct deformations [27, 37], we find all elastic moduli from second- to fifth-order by the least-squares regression using all of the DFT data we have (see supplemental for all DFT data used). The error Z is a weighted sum of two terms related to the energy and PK2 stresses:

$$Z = \frac{1}{6M} \sum_{k=1}^M \sum_{i=1}^6 |S_i^k - S_i^{k0}|^2 + \frac{1}{M} \sum_{k=1}^M w |u_k - u_k^0|^2. \quad (3)$$

Here parameters without superscript 0 designate results from approximate Eqs. (1) and (2) and those with superscript 0 are DFT; M is the number of sets of results of DFT simulations, and w is the weight factor.

Fitted elastic moduli are listed in Tables I and II, with comparison to the third-order elastic potential from other DFT results [24] and experiments [32, 33]. The fourth- and fifth-order elastic moduli have no corresponding parameters from experiments and calculations to compare with. In spite of some deviations (e.g., c_{11} , c_{12} , and c_{123}), the elastic constants are in good overall agreement with the previous DFT and experimental results. As our main focus is on large strain and an elastic instability, we tolerate small discrepancies for small strains, and do not attempt to better fit second- and third-order elastic constant as then stress-strain curves from the elastic potential and DFT will be worse for large strain and the six-order potential will be required.

Validation for energy. Comparing energy contours from the elastic potential and DFT results in the plane of strains $\eta'_1 = \eta'_2$ and η_3 is given in Fig. 1(a) ($\eta'_1 = \eta'_2$ are rotated by 45° around axis 3 coordinate system, as in DFT unit cell [35]). The stress-free Si I from elastic approximation has lattice parameters $a_1 = 3.89 \text{ \AA}$, $c_1 = 5.47 \text{ \AA}$, within 1% of DFT results ($a_1 = 3.8653 \text{ \AA}$, $c_1 = 5.4665 \text{ \AA}$), and close to the recommended value of $5.431\ 020\ 511(89) \text{ \AA}$ [38]. The saddle point (SP: $\eta'_1 = 0.1777$ and $\eta_3 = -0.2584$) has energy 3.2976 J/mm^3

TABLE I. Second- and third-order elastic constants for Si (in GPa), with comparison to other calculations and experiments.

	Present Work	Other Theory[24]	Expt. 1[32]	Expt.2[33]
c_{11}	151.76	162.07	165.04	165.77
c_{12}	59.207	63.51	63.94	63.92
c_{44}	77.90	77.26	79.51	79.62
c_{112}	-455.48	-422	-445±10	-451±5
c_{111}	-653.38	-810	-795±10	-825±10
c_{123}	-95.54	-61	-75±5	-64±10
c_{144}	22.56	31	15±5	12±25
c_{155}	-304.11	-293	-310±5	-310±10
c_{456}	-6.55			

TABLE II. Fourth- and fifth-order elastic constants for Si (in GPa).

c_{1111}	612.74	c_{1112}	2400.94	c_{1122}	1275.11
c_{1123}	1053.03	c_{1144}	5070.79	c_{1155}	4049.80
c_{1255}	-2728.12	c_{1266}	-513.56	c_{1456}	65.5
c_{4455}	-576.86	c_{4444}	-2553.1	c_{11111}	465.42
c_{11112}	-4330.81	c_{11122}	-3442.42	c_{11123}	-3765.50
c_{11155}	-135641.41	c_{11144}	-225996.33	c_{11266}	213.65
c_{12244}	58582.68	c_{11244}	-10255.85	c_{11223}	-1337.79
c_{11456}	1063	c_{12344}	-5924.05	c_{12456}	-1653
c_{14444}	20180.5	c_{14455}	43158.06	c_{15555}	32386.17
c_{15566}	-83526.15	c_{44456}	625.51		

vs. 3.2893 J/mm^3 from DFT. The ability to yield the SP is crucial in capturing the elastic instabilities driving the phase transformation. Furthermore, in Fig. 1(b), the gradients of elastic energy in η'_1 - η_3 plane (with components equal to the PK2 stresses $S'_1 = S'_2$ and S_3) from nonlinear elastic approximation correspond well to those from DFT. Deviations between the analytical results and DFT are quite small. Note that we did not aim to fit points far from the SP toward Si II as they should be fitted to the elastic potential for Si II.

Stress-strain curves for triaxial loading. We compare the Cauchy (true) stress $\sigma_3 - \eta_3$ curves for different fixed lateral stresses $\sigma_1 = \sigma_2$ along the path toward Si I \rightarrow Si II PT (Fig. 2). Corresponding transformation paths in the $(\eta_1 = \eta_2, \eta_3)$ plane are found iteratively using Newton method both for elastic potential and DFT simulations and are presented in [35]. It is clear from Fig. 2 that the fifth-order elastic potential captures the stress-strain curves from DFT calculations correctly for $0 \leq -\eta_3 \leq 0.3$, including peak points of the stress-strain curves, corresponding to elastic instabilities. We use the same definition as in [10]: Elastic lattice instability at prescribed true stress σ occurs at stresses above which the crystal cannot be at equilibrium. All stress-strain curves are smooth, except one for hydrostatic loading. For nonhydrostatic loading, after instability point, elastically distorted tetragonal lattice of Si I continues transformation to tetragonal Si II. However, for

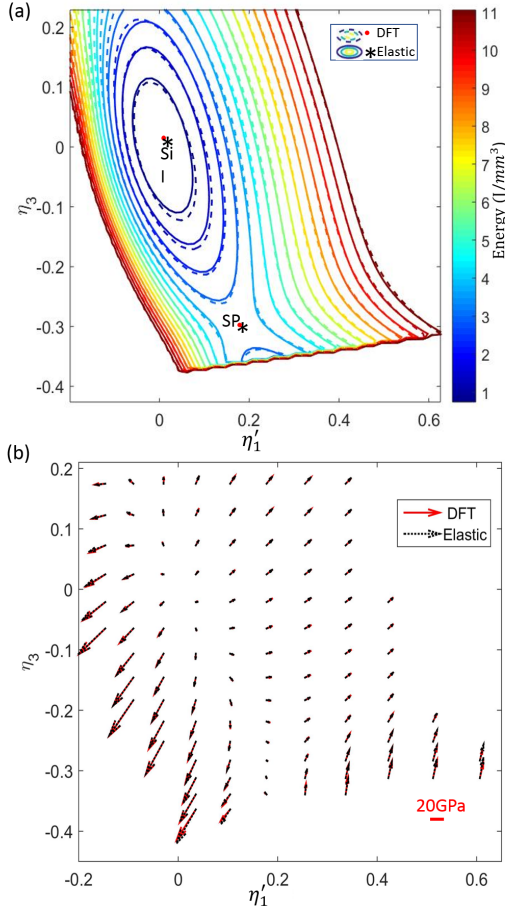


FIG. 1. For Si I, comparison between analytical and DFT results for (a) fifth-order elastic energy and (b) energy gradients in $\eta'_1 = \eta'_2 - \eta_3$ plane. Components of gradients are PK2 stresses $S'_1 = S'_2$ and S_3 .

hydrostatic loading a primary isotropic deformation of cubic Si I is getting unstable with respect to a secondary tetragonal perturbation leading to Si II. Such a bifurcation of the deformation path causes discontinuity of the first derivative at the instability point. This bifurcation and jump in slope are captured correctly in Fig. 2.

Elastic lattice instability criterion under triaxial loading. Combining lattice instability points from DFT and elastic potential, we present the lattice instability criterion in the form of the critical value A of the modified transformation work:

$$W = b_3\sigma_3\epsilon_{t3} + b_1(\sigma_1 + \sigma_2)\epsilon_{t2} = A. \quad (4)$$

Here $\epsilon_{t1} = \epsilon_{t2} = 0.243$ and $\epsilon_{t3} = -0.514$ are transformation strain mapping stress-free crystal lattice of Si I into stress-free lattice of Si II, and b_1 and b_3 are modifying constants. This criterion was derived in [8, 9, 34] via phase field and was verified and quantified by both molecular dynamics simulation using Tersoff potential [8] and DFT simulations [10]. Instability lines can be approximated by $\sigma_3 = 0.4144(\sigma_1 + \sigma_2) - 10.9121$ for nonlinear elasticity and

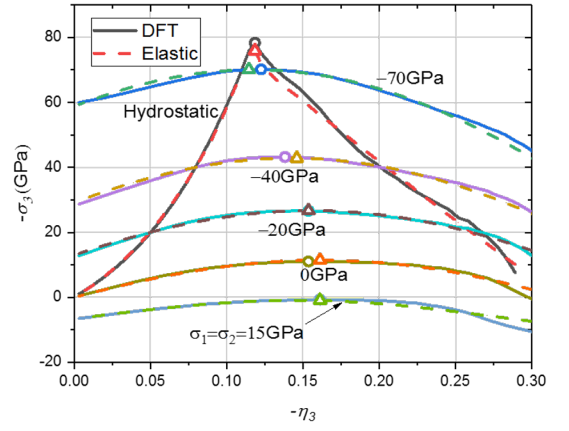


FIG. 2. Cauchy (true) stress vs. Lagrangian strain (σ_3 vs. η_3) for c axis compression or tension for different lateral stresses $\sigma_1 = \sigma_2$ along Si I \rightarrow Si II PT path. DFT (circles) and elastic potential (triangles) designate results with maximum σ_3 . The excellent agreement between elastic potential and DFT is evident.

by $\sigma_3 = 0.4066(\sigma_1 + \sigma_2) - 11.4493$ for DFT results, see supplement [35]. Thus, our fifth-order elastic potential developed here successfully reproduces the lattice instability found in DFT over a range $0.5(\sigma_1 + \sigma_2) \subset [-73.8; 16]$. The strong effect of the nonhydrostatic stresses on the lattice instability is evident: the transformation pressure under hydrostatic loading is ~ 75 GPa and transformation stress σ_3 under uniaxial loading is ~ 11 GPa (or mean stress of 3.7 GPa).

Shear stress-strain curves & instabilities under complex loading: Shear stress-strain curves for simple shears (without normal strains) and for complex loading (shear plus normal strains) are shown in Fig. 3. The elastic shear instability starts at 12.84 GPa (DFT: 12.97) for single shear, reduces to 10.7 GPa (DFT: 11) for double shear ($\eta_4 = \eta_5$), and then to 8.71 GPa (DFT: 8.56) for triple shear, below 3% error with DFT for strains beyond the instability points. Due to symmetry with respect to sign change, there are fewer nonzero elastic constants for shear than for normal strains; for single shear η_4 , $c_{444} = c_{44444} = 0$, and third and fifth degrees of η_4 and η_5 and η_6 are absent. Expectedly, deviation of elastic approximation from DFT grows for strains beyond the shear instability points much faster than for normal strains in Fig. 2. This is not critical, as for unstable branch a phase transformation occurs, which is better described by the order parameter [39, 40]. Note, in a molecular dynamics simulation [15] with a Stillinger-Weber potential [41], the instability for simple shear along $\langle \bar{1}\bar{1}2 \rangle$ in the (111) plane and along the $\langle 111 \rangle$ in the $(\bar{1}\bar{1}0)$ plane lead to amorphization.

Note that double and triple shears along the $\langle 100 \rangle$ in the (001) plane in Fig. 3(a) represent single shear in $\langle 110 \rangle$ in the (001) plane with $\eta'_4 = \sqrt{2}\eta_4$ and triaxial normal-strain loading in $\langle 111 \rangle$ and in the (111) plane with $\eta'_1 = 2\eta_4$ and $\eta'_2 = \eta_3 = -\eta_4$, respectively. Then curves in Fig. 3(a) can be analyzed in terms of the effect of crystallographic anisotropy. Generally, by rotating coordinate system and transforming

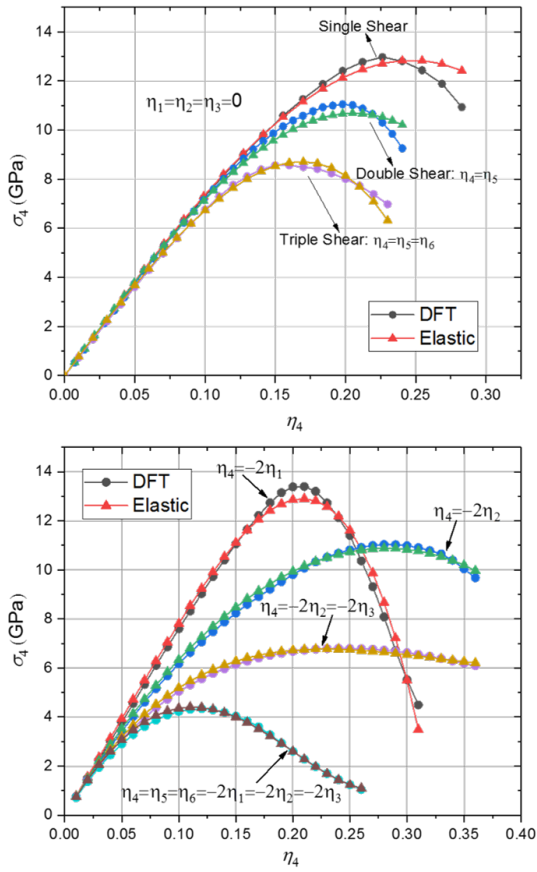


FIG. 3. True shear stress–strain curves from 5^{th} -order elastic potential compared to DFT results: for (a) single, double, and triple shear strains ($\eta_1 = \eta_2 = \eta_3 = 0$); (b) combination of normal and shear strains (all non-mentioned strains are zero). Fifth-order potential describes DFT results well, including shear instabilities.

elastic potential accordingly, one can study the effect of the anisotropy for an arbitrary complex loading.

For the shearing in combination with compressive normal strains (Fig. 3(b)), the DFT results are described by our elastic potential even better than just for shearing, i.e., with smaller deviation for larger strains even exceeding 0.35. Interestingly, superposing uniaxial compression $\eta_1 = -0.5\eta_4$ orthogonal to shear plane in Fig. 3(b) slightly increases ultimate (theoretical) shear strength but slightly reduces corresponding shear strain in comparison with Fig. 3(a). At the same time, superposing uniaxial compression $\eta_2 = -0.5\eta_4$ in the shear η_4 direction reduces ultimate shear strength by ~ 2 GPa, but increases corresponding shear strain. Superposing biaxial compression $\eta_1 = \eta_2 = -0.5\eta_4$ further reduces ultimate shear strength down to 6.77 GPa (6.79 from DFT) with corresponding shear strain between two previous cases. Shape of shear stress-strain curves changes also significantly with superposition of different compressive strains. Also, superposing isotropic compression $\eta_1 = \eta_2 = \eta_3 = -0.5\eta_4 = -0.5\eta_5 = -0.5\eta_6$ on the triple shearing reduces ultimate shear strength from 8.71 GPa (8.56 from DFT) in Fig. 3(a) to 4.4 GPa

(4.31 from DFT) in Fig. 3(b) and also strongly reduces corresponding shear strain. The tendency in reducing shear stability under hydrostatic loading in combination with presence of the dislocations with local stress concentrators may lead to pressure-induced amorphization observed experimentally [42]. The observed coupling between shear and normal stresses is very nontrivial and well captured. Typically, shear instabilities do not lead to Si II but rather to possible amorphization, hexagonal diamond Si IV, slip, or twinning.

Note that presence of the plateau-like portion in the stress-strain curves for diamond was coined in [43] as "atomic plasticity" and was considered as an indicator of desired combination of high strength with sufficient ductility. Such an atomic ductility is observed for Si under compression (Fig. 2 (a)) but not for shears (Fig. 3(a)). However, superposition of certain normal strains (e.g., $\eta_2 = -0.5\eta_4$ and especially $\eta_1 = \eta_2 = -0.5\eta_4$) significantly increases plateau.

In summary, the fifth-degree elastic potential for Si I under large strain including instability points was obtained in terms of Lagrangian strains by minimizing error relative to DFT results. Elastic energy and true stress-strain curves for arbitrary complex loadings (including elastic instability) reproduce DFT results very well. Phase transition conditions for Si I \rightarrow Si II under three normal cubic stresses are found to be linear in true stresses, in perfect agreement with DFT. Any lower-order potentials (less than fifth-degree) cannot derive a similar precision in description of elastic instabilities and stress-strain curves, whereas, in contrast, they are currently found mostly using third-order elastic constants determined at small strains. Our results also show the potential of controlling the stress-strain curves and phase transitions by applying optimized, multidimensional loading to control desirable properties and to drastically reduce phase transition pressures (1–2 orders of magnitude) [10, 17, 31, 44].

Besides being generally applicable, the elastic potential contains in convenient analytical form a plethora of information and now permits a direct study of all elastic instabilities under complex loading driving different phase transitions (allotropic, amorphization, and melting), fracture, slip, and twinning. Using higher-order potentials and large strains that include instabilities yields qualitatively and quantitatively better predictive capability, improving the entire model-based simulations, which are much faster than DFT. Notably, our approach represents a fundamentally new basis for continuum simulations of crystal behavior under extreme static and dynamic loadings involving multiple the above mentioned orientational-dependent mechanisms. In particular, higher-order elasticity is required for determination of the stress-strain states and optimization of the diamond anvil cell for reaching maximum possible pressures [21]. This approach is general and will significantly improve phase fields models of phase transformations, in contrast to second-order elasticity used currently [39, 40, 45]. It also provides a basis for the description of the competition between different instabilities at different loadings.

Acknowledgements: VIL and HC are supported by NSF

(CMMI-1536925 & MMN-1904830), ARO (W911NF-17-1-0225), ONR (N00014-16-1-2079), & XSEDE (MSS170015). NAZ and DDJ are supported by the U.S. Department of Energy (DOE), Office of Science, Basic Energy Sciences, Materials Science & Engineering Division. Ames Laboratory is operated for DOE by Iowa State University under contract DE-AC02-07CH11358.

* chen hao.hitgucas@gmail.com

† zarkev@ameslab.gov

‡ vlevitas@iastate.edu

§ ddj@iastate.edu, ddj@ameslab.gov

¶ xc Zhang@ecust.edu.cn

- [1] Rodney Hill and Frederick Milstein, "Principles of stability analysis of ideal crystals," *Phys. Rev. B* **15**, 3087 (1977).
- [2] Göran Grimvall, Blanka Magyari-Köpe, Vidvuds Ozoliņš, and Kristin A Persson, "Lattice instabilities in metallic elements," *Rev. Mod. Phys.* **84**, 945 (2012).
- [3] Maarten De Jong, Ian Winter, DC Chrzan, and Mark Asta, "Ideal strength and ductility in metals from second- and third-order elastic constants," *Phys. Rev. B* **96**, 014105 (2017).
- [4] J Pokluda, M Černý, M Šob, and Y Umeno, "Ab initio calculations of mechanical properties: Methods and applications," *Prog. Mater. Sci.* **73**, 127–158 (2015).
- [5] RS Telyatnik, AV Osipov, and SA Kukushkin, "Ab initio modelling of nonlinear elastoplastic properties of diamond-like c, sic, si, ge crystals upon large strains," *Mater. Phys. & Mech.* **29** (2016).
- [6] Jinghan Wang, Sidney Yip, SR Phillpot, and Dieter Wolf, "Crystal instabilities at finite strain," *Phys. Rev. Lett.* **71**, 4182 (1993).
- [7] Kazuki Mizushima, Sidney Yip, and Efthimios Kaxiras, "Ideal crystal stability and pressure-induced phase transition in silicon," *Phys. Rev. B* **50**, 14952 (1994).
- [8] Valery I Levitas, Hao Chen, and Liming Xiong, "Lattice instability during phase transformations under multiaxial stress: Modified transformation work criterion," *Phys. Rev. B* **96**, 054118 (2017).
- [9] Valery I Levitas, Hao Chen, and Liming Xiong, "Triaxial-stress-induced homogeneous hysteresis-free first-order phase transformations with stable intermediate phases," *Phys. Rev. Lett.* **118**, 025701 (2017).
- [10] Nikolai A Zarkevich, Hao Chen, Valery I Levitas, and Duane D Johnson, "Lattice instability during solid-solid structural transformations under a general applied stress tensor: Example of si to si ii with metallization," *Phys. Rev. Lett.* **121**, 165701 (2018).
- [11] N Binggeli and James R Chelikowsky, "Elastic instability in α -quartz under pressure," *Phys. Rev. Lett.* **69**, 2220 (1992).
- [12] Kathleen J Kingma, Charles Meade, Russell J Hemley, Howkwang Mao, and David R Veblen, "Microstructural observations of α -quartz amorphization," *Science* **259**, 666–669 (1993).
- [13] VV Brazhkin and AG Lyapin, "Lattice instability approach to the problem of high-pressure solid-state amorphization," *High Press. Res.* **15**, 9–30 (1996).
- [14] S Zhao, R Flanagan, EN Hahn, B Kad, BA Remington, CE Wehrenberg, R Cauble, K More, and MA Meyers, "Shock-induced amorphization in silicon carbide," *Acta Mater.* **158**, 206–213 (2018).
- [15] Hao Chen, Valery I Levitas, and Liming Xiong, "Amorphization induced by 60° shuffle dislocation pileup against different grain boundaries in silicon bicrystal under shear," *Acta Mater.* **179**, 287–295 (2019).
- [16] J L Tallon, "A hierarchy of catastrophes as a succession of stability limits for the crystalline state," *Nature* **342**, 658 (1989).
- [17] Valery I Levitas and Ramon Ravelo, "Virtual melting as a new mechanism of stress relaxation under high strain rate loading," *Proc. Natl. Acad. Sci. U.S.A.* **109**, 13204–13207 (2012).
- [18] Yoshitaka Umeno and Miroslav Černý, "Effect of normal stress on the ideal shear strength in covalent crystals," *Phys. Rev. B* **77**, 100101 (2008).
- [19] Miroslav Černý, Petr Řehák, Yoshitaka Umeno, and Jaroslav Pokluda, "Stability and strength of covalent crystals under uniaxial and triaxial loading from first principles," *J. Phys. Condens. Matter* **25**, 035401 (2012).
- [20] Meijie Tang and Sidney Yip, "Lattice instability in β -sic and simulation of brittle fracture," *J. Appl. Phys.* **76**, 2719–2725 (1994).
- [21] Valery I Levitas, Mehdi Kamrani, and Biao Feng, "Tensorial stress-strain fields and large elastoplasticity as well as friction in diamond anvil cell up to 400 gpa," *npj Comput. Mater.* **5**, 1–11 (2019).
- [22] John D Clayton, "Analysis of shock compression of strong single crystals with logarithmic thermoelastic-plastic theory," *Int. J. Eng. Sci.* **79**, 1–20 (2014).
- [23] John D Clayton, "Crystal thermoelasticity at extreme loading rates and pressures: analysis of higher-order energy potentials," *Extreme Mech. Lett.* **3**, 113–122 (2015).
- [24] Jijun Zhao, J. M. Winey, and Y. M. Gupta, "First-principles calculations of second- and third-order elastic constants for single crystals of arbitrary symmetry," *Phys. Rev. B* **75**, 094105 (2007).
- [25] Michał Łopuszyński and Jacek A Majewski, "Ab initio calculations of third-order elastic constants and related properties for selected semiconductors," *Phys. Rev. B* **76**, 045202 (2007).
- [26] Tengfei Cao, David Cuffari, and Angelo Bongiorno, "First-principles calculation of third-order elastic constants via numerical differentiation of the second piola-kirchhoff stress tensor," *Phys. Rev. Lett.* **121**, 216001 (2018).
- [27] Hao Wang and Mo Li, "Ab initio calculations of second-, third-, and fourth-order elastic constants for single crystals," *Phys. Rev. B* **79**, 224102 (2009).
- [28] Arsenii V Telichko, Sergey V Erohin, Gennady M Kvashnin, Pavel B Sorokin, Boris P Sorokin, and Vladimir D Blank, "Diamonds third-order elastic constants: Ab initio calculations and experimental investigation," *J. Mater. Sci.* **52**, 3447–3456 (2017).
- [29] Dezhou Guo and Qi An, "Transgranular amorphous shear band formation in polycrystalline boron carbide," *Int. J. Plast.* **121**, 218–226 (2019).
- [30] Qi An, William A Goddard III, and Tao Cheng, "Atomistic explanation of shear-induced amorphous band formation in boron carbide," *Phys. Rev. Lett.* **113**, 095501 (2014).
- [31] Yang Gao, Yanzhang Ma, Qi An, Valery Levitas, Yanyan Zhang, Biao Feng, Jharna Chaudhuri, and William A Goddard III, "Shear driven formation of nano-diamonds at sub-gigapascals and 300 k," *Carbon* **146**, 364–368 (2019).
- [32] John J Hall, "Electronic effects in the elastic constants of n-type silicon," *Phys. Rev.* **161**, 756 (1967).
- [33] HJ McSkimin and P Andreatch Jr, "Measurement of third-order moduli of silicon and germanium," *J. App. Phys.* **35**, 3312–3319 (1964).
- [34] Valery I Levitas, "Phase-field theory for martensitic phase

- transformations at large strains,” *Inter. J. Plast.* **49**, 85–118 (2013).
- [35] See Supplemental Material at [URL will be inserted by publisher] for data sets for all figures, simulation methods, and explicit expression of the fifth-degree elastic potential for cubic crystals.
- [36] Cristian Teodosiu, *Elastic models of crystal defects* (Springer Science & Business Media, 2013).
- [37] Igor Mosyagin, AV Lugovskoy, OM Krasilnikov, Yu Kh Vekilov, SI Simak, and IA Abrikosov, “Ab initio calculations of pressure-dependence of high-order elastic constants using finite deformations approach,” *Comput. Phys. Commun.* **220**, 20–30 (2017).
- [38] Eite Tiesinga, Peter J. Mohr, David B. Newell, and Barry N. Taylor, *The 2018 CODATA Recommended Values of the Fundamental Physical Constants* (National Institute of Standards and Technology, Gaithersburg, MD 20899, USA, 2020) NIST database developed by J. Baker, M. Douma, and S. Kotchigova.
- [39] Valery I Levitas, “Phase field approach for stress-and temperature-induced phase transformations that satisfies lattice instability conditions. part i. general theory,” *Inter. J. Plast.* **106**, 164–185 (2018).
- [40] Hamed Babaei and Valery I Levitas, “Phase-field approach for stress-and temperature-induced phase transformations that satisfies lattice instability conditions. part 2. simulations of phase transformations si i - si ii,” *Inter. J. Plast.* **107**, 223–245 (2018).
- [41] Frank H Stillinger and Thomas A Weber, “Computer simulation of local order in condensed phases of silicon,” *Phys. Rev. B* **31**, 5262 (1985).
- [42] Sudip K Deb, Martin Wilding, Maddury Somayazulu, and Paul F McMillan, “Pressure-induced amorphization and an amorphous–amorphous transition in densified porous silicon,” *Nature* **414**, 528 (2001).
- [43] Chang Liu, Xianqi Song, Quan Li, Yanming Ma, and Changfeng Chen, “Smooth flow in diamond: Atomistic ductility and electronic conductivity,” *Phys. Rev. Lett.* **123**, 195504 (2019).
- [44] Cheng Ji, Valery I Levitas, Hongyang Zhu, Jharna Chaudhuri, Archis Marathe, and Yanzhang Ma, “Shear-induced phase transition of nanocrystalline hexagonal boron nitride to wurtzitic structure at room temperature and lower pressure,” *PNAS* **109**, 19108–19112 (2012).
- [45] Hamed Babaei and Valery I Levitas, “Stress-measure dependence of phase transformation criterion under finite strains: Hierarchy of crystal lattice instabilities for homogeneous and heterogeneous transformations,” *Phys. Rev. Lett.* , in press (2020).

SUPPLEMENTAL MATERIAL

Fifth-degree elastic potential for predictive stress-strain relations and elastic instabilities under large strain and complex loading in Si

Hao Chen,^{1,*} Nikolai A. Zarkevich,^{2,†} Valery I. Levitas,^{2,3,4,5,‡} Duane D. Johnson,^{2,5,§} and Xiancheng Zhang¹

¹*Key Laboratory of Pressure Systems and Safety,
Ministry of Education, School of Mechanical and Power Engineering,
East China University of Science and Technology, Shanghai 200237, China*

²*Ames Laboratory, U.S. Department of Energy,
Iowa State University, Ames, Iowa 50011-3020, USA*

³*Department of Aerospace Engineering,
Iowa State University, Ames, Iowa 50011, USA*

⁴*Department of Mechanical Engineering,
Iowa State University, Ames, Iowa 50011, USA*

⁵*Department of Materials Science & Engineering,
Iowa State University, Ames, Iowa 50011, USA*

I. SIMULATION METHODS

We used DFT as implemented in VASP [1–3] with the projector augmented waves (PAW) basis [4, 5] and PBE exchange-correlation functional [6]. The PAW-PBE pseudo-potential of Si had 4 valence electrons (s^2p^2) and 1.9 Å cutoff radius. The plane-wave energy cutoff (ENCUT) was 306.7 eV, while the cut-off energy of the plane wave representation of the augmentation charges (ENAUG) was 322.1 eV. We used a Davidson block iteration scheme (IALGO=38) for the electronic energy minimization. Electronic structure was calculated with a fixed number of bands (NBANDS=16) in a tetragonal 4-atom unit cell (a supercell of a 2-atom primitive cell). Brillouin zone integrations were done in k -space (LREAL=FALSE) using a Γ -centered Monkhorst-Pack mesh [7] containing 55 to 110 k -points per Å⁻¹ (fewer during atomic relaxation, more for the final energy calculation). Accelerated convergence of the self-consistent calculations was achieved using a modified Broyden’s method [8].

Atomic relaxation in a fixed unit cell (ISIF=2) was performed using the conjugate gradient algorithm (IBRION=2), allowing symmetry breaking (ISYM=0). The transformation path was confirmed by the nudged-elastic band (NEB) calculations, performed using the C2NEB code [9]. We used DFT forces in *ab initio* molecular dynamics (MD) to verify stability of the relaxed atomic structures. Si atoms were assumed to have mass POMASS=28.085 atomic mass units (amu). The time step for the atomic motion was set to POTIM=0.5 fs. Convergence vs. plane-wave energy cutoff is discussed in [10]. The converged DFT data contained over 10⁴ entries and was processed in the format, outlined in Table 3 in [11].

The unit cells in the DFT simulations contained 4 atoms and were oriented along $A^* = \langle 110 \rangle$, $B^* = \langle 1\bar{1}0 \rangle$, and $C^* = \langle 001 \rangle$. The transformation matrix for transforming the current simulation coordinate system to the natural 8-atom cubic cell, oriented along $A = \langle 100 \rangle$, $B = \langle 010 \rangle$, and $C = \langle 001 \rangle$, is:

$$R = [A, B, C][A^*, B^*, C^*]^{-1} = \begin{bmatrix} 1/\sqrt{2} & -1/\sqrt{2} & 0 \\ 1/\sqrt{2} & 1/\sqrt{2} & 0 \\ 0 & 0 & 1 \end{bmatrix} \quad (\text{S1})$$

The transformation formulas of the deformation gradient and Cauchy and second Piola-Kirchhoff (PK2) stresses to the natural cubic coordinate system are

$$F = R * F^* * R^T; \quad \sigma = R * \sigma^* * R^T; \quad S = R * S^* * R^T. \quad (\text{S2})$$

Parameter identification procedure is carried out and results are presented in the natural cubic

coordinate system.

II. FIFTH-ORDER ELASTIC ENERGY FORMULA FOR CUBIC SYSTEMS

The fifth-order energy for cubic symmetry can be expressed as

$$u = \psi_2 + \psi_3 + \psi_4 + \psi_5 + \dots \quad (\text{S3})$$

in which

$$\psi_2 = \frac{1}{2}c_{111}(\eta_1^2 + \eta_2^2 + \eta_3^2) + c_{112}(\eta_1\eta_2 + \eta_2\eta_3 + \eta_1\eta_3) + \frac{1}{2}c_{444}(\eta_4^2 + \eta_5^2 + \eta_6^2) \quad (\text{S4})$$

$$\begin{aligned} \psi_3 = & \frac{1}{6}c_{111}(\eta_1^3 + \eta_2^3 + \eta_3^3) + \frac{1}{2}c_{112}[\eta_1^2(\eta_2 + \eta_3) + \eta_2^2(\eta_1 + \eta_3) + \eta_3^2(\eta_1 + \eta_2)] + \\ & \frac{1}{2}c_{155}[\eta_4^2(\eta_2 + \eta_3) + \eta_5^2(\eta_1 + \eta_3) + \eta_6^2(\eta_1 + \eta_2)] + c_{456}\eta_4\eta_5\eta_6 + c_{123}\eta_1\eta_2\eta_3 + \\ & \frac{1}{2}c_{144}(\eta_1\eta_4^2 + \eta_2\eta_5^2 + \eta_3\eta_6^2) \end{aligned} \quad (\text{S5})$$

$$\begin{aligned} \psi_4 = & \frac{1}{4}c_{1122}(\eta_1^2\eta_2^2 + \eta_2^2\eta_3^2 + \eta_1^2\eta_3^2) + \frac{1}{6}c_{1112}[\eta_1^3(\eta_2 + \eta_3) + \eta_2^3(\eta_1 + \eta_3) + \eta_3^3(\eta_1 + \eta_2)] + \\ & \frac{1}{24}c_{1111}(\eta_1^4 + \eta_2^4 + \eta_3^4) + \frac{1}{2}c_{1123}\eta_1\eta_2\eta_3(\eta_1 + \eta_2 + \eta_3) + \frac{1}{4}c_{1144}(\eta_1^2\eta_4^2 + \eta_2^2\eta_5^2 + \eta_3^2\eta_6^2) + \\ & \frac{1}{4}c_{1155}[\eta_1^2(\eta_5^2 + \eta_6^2) + \eta_2^2(\eta_6^2 + \eta_4^2) + \eta_3^2(\eta_5^2 + \eta_4^2)] + \frac{1}{2}c_{1266}(\eta_1\eta_2\eta_6^2 + \eta_2\eta_3\eta_4^2 + \eta_1\eta_3\eta_5^2) \quad (\text{S6}) \\ & \frac{1}{2}c_{1255}[\eta_1\eta_2(\eta_4^2 + \eta_5^2) + \eta_2\eta_3(\eta_5^2 + \eta_6^2) + \eta_1\eta_3(\eta_4^2 + \eta_6^2)] + \frac{1}{4}c_{4455}(\eta_4^2\eta_5^2 + \eta_5^2\eta_6^2 + \eta_4^2\eta_6^2) + \\ & c_{1456}\eta_4\eta_5\eta_6(\eta_1 + \eta_2 + \eta_3) + \frac{1}{24}c_{4444}(\eta_4^4 + \eta_5^4 + \eta_6^4) + \frac{1}{2}c_{1266}(\eta_1\eta_2\eta_6^2 + \eta_2\eta_3\eta_4^2 + \eta_1\eta_3\eta_5^2) \end{aligned}$$

$$\begin{aligned}
\psi_5 = & \frac{1}{120}c_{11111}(\eta_1^5 + \eta_2^5 + \eta_3^5) + \frac{1}{2}c_{11456}\eta_4\eta_5\eta_6(\eta_1^2 + \eta_2^2 + \eta_3^2) + \frac{1}{2}c_{12344}\eta_1\eta_2\eta_3(\eta_4^2 + \eta_5^2 + \eta_6^2) + \\
& \frac{1}{24}c_{15555}[\eta_1(\eta_5^4 + \eta_6^4) + \eta_2(\eta_4^4 + \eta_6^4) + \eta_3(\eta_4^4 + \eta_5^4)] + \frac{1}{4}c_{11223}(\eta_1\eta_2^2\eta_3^2 + \eta_1^2\eta_2\eta_3^2 + \eta_1^2\eta_2^2\eta_3) \\
& \frac{1}{24}c_{14444}(\eta_1\eta_4^4 + \eta_2\eta_5^4 + \eta_3\eta_6^4) + \frac{1}{4}c_{14455}[\eta_1\eta_4^2(\eta_5^2 + \eta_6^2) + \eta_2\eta_5^2(\eta_4^2 + \eta_6^2) + \eta_3\eta_6^2(\eta_4^2 + \eta_5^2)] + \\
& \frac{1}{12}c_{11122}[\eta_1^3(\eta_2^2 + \eta_3^2) + \eta_2^3(\eta_1^2 + \eta_3^2) + \eta_3^3(\eta_1^2 + \eta_2^2)] + \frac{1}{6}c_{11123}(\eta_1^3\eta_2\eta_3 + \eta_1\eta_2^3\eta_3 + \eta_1\eta_2\eta_3^3) + \\
& \frac{1}{12}c_{11155}[\eta_1^3(\eta_5^2 + \eta_6^2) + \eta_2^3(\eta_4^2 + \eta_6^2) + \eta_3^3(\eta_4^2 + \eta_5^2)] + \frac{1}{12}c_{11144}(\eta_1^3\eta_4^2 + \eta_2^3\eta_5^2 + \eta_3^3\eta_6^2) + \\
& c_{12456}\eta_4\eta_5\eta_6(\eta_1\eta_2 + \eta_1\eta_3 + \eta_2\eta_3) + \frac{1}{24}c_{11112}[\eta_1^4(\eta_2 + \eta_3) + \eta_2^4(\eta_1 + \eta_3) + \eta_3^4(\eta_1 + \eta_2)] + \\
& \frac{1}{4}c_{11266}[\eta_1\eta_2(\eta_2 + \eta_1)\eta_6^2 + \eta_1\eta_3(\eta_1 + \eta_3)\eta_5^2 + \eta_2\eta_3(\eta_2 + \eta_3)\eta_4^2] + \\
& \frac{1}{4}c_{15566}(\eta_3\eta_4^2\eta_5^2 + \eta_2\eta_4^2\eta_6^2 + \eta_1\eta_5^2\eta_6^2) + \frac{1}{6}c_{44456}\eta_4\eta_5\eta_6(\eta_4^2 + \eta_5^2 + \eta_6^2) + \\
& \frac{1}{4}c_{12244}[\eta_1(\eta_2^2 + \eta_3^2)\eta_4^2 + \eta_2(\eta_1^2 + \eta_3^2)\eta_5^2 + \eta_3(\eta_1^2 + \eta_2^2)\eta_6^2] + \\
& \frac{1}{4}c_{11244}[\eta_1^2(\eta_2 + \eta_3)\eta_4^2 + \eta_2^2(\eta_1 + \eta_3)\eta_5^2 + \eta_3^2(\eta_2 + \eta_1)\eta_6^2]
\end{aligned} \tag{S7}$$

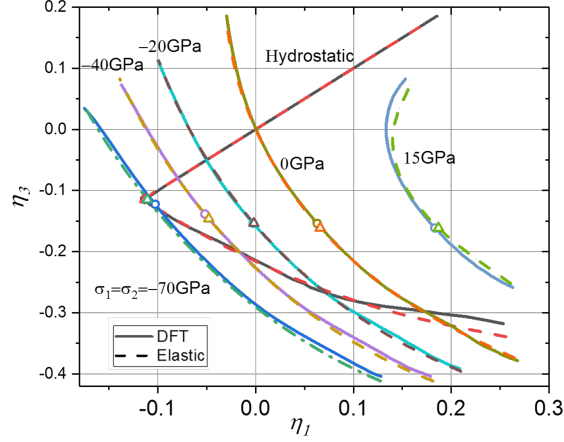


FIG. S1. Comparison of the loading paths obtained using DFT simulations and elastic potential in the $(\eta_1 = \eta_2, \eta_3)$ plane for compression/tension along η_3 for different fixed stresses $\sigma_1 = \sigma_2$ corresponding to the results in Fig. 2 of the main text. The "hydrostatic" line designates loading path for $\sigma_1 = \sigma_2 = \sigma_3$.

III. SOME ADDITIONAL RESULTS

Comparison of the loading paths corresponding to compression or tension along η_3 at different fixed stresses $\sigma_1 = \sigma_2$ from nonlinear elastic approximation and DFT results is presented in Fig. S1. Good correspondence is evident. These paths are used to obtain stress σ_3 vs. Lagrangian strain η_3 dependence in Fig. 2 of the main text.

Lattice instability lines under triaxial compression stress states for PT Si I \rightarrow Si II are presented in Fig. S2. They are approximated by linear function in the main text. Again, they practically coincide.

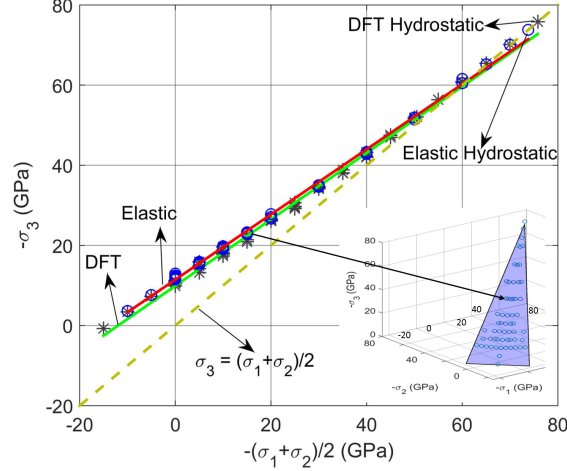


FIG. S2. Comparison of the elastic instability condition σ_3 versus $0.5(\sigma_1 + \sigma_2)$ for Si I \rightarrow Si II PT from the fifth-order elastic potential (circles) and DFT results (*). The inset shows the same instability points from the fifth-order elastic potential (circles) in 3D space σ_1 , σ_2 , and σ_3 , which lie very close to the instability plane calibrated with DFT in [10].

* chenhao.hitgucas@gmail.com

† zarkev@ameslab.gov

‡ vlevitas@iastate.edu

§ ddj@iastate.edu, ddj@ameslab.gov

¹ Georg Kresse and Jürgen Hafner, “Ab initio molecular dynamics for liquid metals,” *Phys. Rev. B* **47**, 558 (1993).

² Georg Kresse and Jürgen Hafner, “Ab initio molecular-dynamics simulation of the liquid-metal–amorphous-semiconductor transition in germanium,” *Phys. Rev. B* **49**, 14251 (1994).

³ Georg Kresse and Jürgen Furthmüller, “Efficiency of ab-initio total energy calculations for metals and semiconductors using a plane-wave basis set,” *Computational materials science* **6**, 15–50 (1996).

⁴ Peter E Blöchl, “Projector augmented-wave method,” *Phys. Rev. B* **50**, 17953 (1994).

⁵ Georg Kresse and D Joubert, “From ultrasoft pseudopotentials to the projector augmented-wave method,” *Physical Review B* **59**, 1758 (1999).

⁶ John P Perdew, Kieron Burke, and Matthias Ernzerhof, “Generalized gradient approximation made simple,” *Phys. Rev. Lett.* **77**, 3865 (1996).

- ⁷ Hendrik J Monkhorst and James D Pack, “Special points for brillouin-zone integrations,” *Phys. Rev. B* **13**, 5188 (1976).
- ⁸ Duane D Johnson, “Modified broydens method for accelerating convergence in self-consistent calculations,” *Phys. Rev. B* **38**, 12807 (1988).
- ⁹ N A Zarkevich and D D Johnson, “Nudged-elastic band method with two climbing images: finding transition states in complex energy landscapes,” *J. Chem. Phys.* **142**, 024106 (2015).
- ¹⁰ Nikolai A Zarkevich, Hao Chen, Valery I Levitas, and Duane D Johnson, “Lattice instability during solid-solid structural transformations under a general applied stress tensor: Example of si i to si ii with metallization,” *Phy. Rev. Lett.* **121**, 165701 (2018).
- ¹¹ N. A. Zarkevich, “Structural database for reducing cost in materials design and complexity of multiscale computations,” *Complexity* **11**, 36–42 (2006).